Graphene-based tunable broadband hyperlens for far-field subdiffraction imaging at mid-infrared frequencies

Tian Zhang,[1] Lin Chen,[1,*] and Xun Li[2]

[1]*Wuhan National Laboratory for Optoelectronics, Huazhong University of Science and Technology, Wuhan 430074, China*
[2]*Department of Electrical and Computer Engineering, McMaster University, 1280 Main Street West, Hamilton, Ontario, L8S 4L8 Canada*
[*]*chen.lin@mail.hust.edu.cn*

Abstract: Considering the dielectric permittivity of graphene can be tuned to be negative by external electric field, we propose to construct alternating graphene/dielectric multilayer based optical hyperlens for far-field subdiffraction imaging at mid-infrared frequencies. For such a scheme, hyperbolic dispersion curve can be achieved under the condition that the thickness of dielectric layer is made comparable to that of graphene layer, which is capable of supporting the propagation of evanescent wave with large wave vector. Simulation results by finite-element method demonstrate that two point sources with separation far below the diffraction limit can be magnified by the systems to the extent that conventional far-field optical microscopy can further manipulate. Such a hyperlens has the advantage of operating in a wideband region due to the tunability of graphene's dielectric permittivity as opposed to previous metal based hyperlens, enabling the potential applications in real-time super-resolution imaging, nanolithography, and sensing.

References and links

1. E. Abbe, "Beiträge zur Theorie des Mikroskops und der mikroskopischen Wahrnehmung," Arch. Mikrosk. Anat. **9**(1), 413–418 (1873).
2. U. Dürig, D. Pohl, and F. Rohner, "Near-field optical-scanning microscopy," J. Appl. Phys. **59**(10), 3318–3327 (1986).
3. W. L. Barnes, A. Dereux, and T. W. Ebbesen, "Surface plasmon subwavelength optics," Nature **424**(6950), 824–830 (2003).
4. R. F. Oulton, V. J. Sorger, D. A. Genov, D. F. P. Pile, and X. Zhang, "A hybrid plasmonic waveguide for subwavelength confinement and long-range propagation," Nat. Photonics **2**(8), 496–500 (2008).
5. M. Z. Alam, J. S. Aitchison, and M. Mojahedi, "Compact and silicon-on-insulator-compatible hybrid plasmonic TE-pass polarizer," Opt. Lett. **37**(1), 55–57 (2012).
6. L. Chen, X. Li, G. P. Wang, W. Li, S. H. Chen, L. Xiao, and D. S. Gao, "A silicon-based 3-D hybrid long-range plasmonic waveguide for nanophotonic integration," J. Lightwave Technol. **30**(1), 163–168 (2012).
7. L. Chen, T. Zhang, X. Li, and W. P. Huang, "Novel hybrid plasmonic waveguide consisting of two identical dielectric nanowires symmetrically placed on each side of a thin metal film," Opt. Express **20**(18), 20535–20544 (2012).
8. L. Chen, X. Li, and G. P. Wang, "A hybrid long-range plasmonic waveguide with sub-wavelength confinement," Opt. Commun. **291**, 400–404 (2013).
9. M. I. Stockman, "Nanofocusing of optical energy in tapered plasmonic waveguides," Phys. Rev. Lett. **93**(13), 137404 (2004).
10. L. Chen and G. Wang, "Nanofocusing of light energy by ridged metal heterostructures," Appl. Phys. B **89**(4), 573–577 (2007).
11. J. B. Pendry, "Negative refraction makes a perfect lens," Phys. Rev. Lett. **85**(18), 3966–3969 (2000).
12. N. Fang, H. Lee, C. Sun, and X. Zhang, "Sub-diffraction-limited optical imaging with a silver superlens," Science **308**(5721), 534–537 (2005).

13. Z. Jacob, L. V. Alekseyev, and E. Narimanov, "Optical hyperlens: far-field imaging beyond the diffraction limit," Opt. Express **14**(18), 8247–8256 (2006).
14. A. Salandrino and N. Engheta, "Far-field subdiffraction optical microscopy using metamaterial crystals: theory and simulations," Phys. Rev. B **74**(7), 075103 (2006).
15. Z. Liu, H. Lee, Y. Xiong, C. Sun, and X. Zhang, "Far-field optical hyperlens magnifying sub-diffraction-limited objects," Science **315**(5819), 1686 (2007).
16. L. Chen, X. Zhou, and G. Wang, "V-shaped metal–dielectric multilayers for far-field subdiffraction imaging," Appl. Phys. B **92**(2), 127–131 (2008).
17. L. Chen and G. P. Wang, "Pyramid-shaped hyperlenses for three-dimensional subdiffraction optical imaging," Opt. Express **17**(5), 3903–3912 (2009).
18. K. L. Tsakmakidis, A. D. Boardman, and O. Hess, "'Trapped rainbow' storage of light in metamaterials," Nature **450**(7168), 397–401 (2007).
19. Q. Gan, Z. Fu, Y. J. Ding, and F. J. Bartoli, "Ultrawide-bandwidth slow-light system based on THz plasmonic graded metallic grating structures," Phys. Rev. Lett. **100**(25), 256803 (2008).
20. L. Chen, G. P. Wang, X. Li, W. Li, Y. Shen, J. Lai, and S. Chen, "Broadband slow-light in graded-grating-loaded plasmonic waveguides at telecom frequencies," Appl. Phys. B **104**(3), 653–657 (2011).
21. H. Hu, D. Ji, X. Zeng, K. Liu, and Q. Gan, "Rainbow trapping in hyperbolic metamaterial waveguide," Sci. Rep. **3**, 1249 (2013).
22. Y. Xiong, Z. Liu, C. Sun, and X. Zhang, "Two-dimensional imaging by far-field superlens at visible wavelengths," Nano Lett. **7**(11), 3360–3365 (2007).
23. S. Kawata, A. Ono, and P. Verma, "Subwavelength colour imaging with a metallic nanolens," Nat. Photonics **2**(7), 438–442 (2008).
24. Z. Jacob, L. V. Alekseyev, and E. Narimanov, "Semiclassical theory of the hyperlens," J. Opt. Soc. Am. A **24**(10), A52–A59 (2007).
25. H. Lee, Z. Liu, Y. Xiong, C. Sun, and X. Zhang, "Development of optical hyperlens for imaging below the diffraction limit," Opt. Express **15**(24), 15886–15891 (2007).
26. J. Li, L. Fok, X. Yin, G. Bartal, and X. Zhang, "Experimental demonstration of an acoustic magnifying hyperlens," Nat. Mater. **8**(12), 931–934 (2009).
27. X. Zhang and Z. Liu, "Superlenses to overcome the diffraction limit," Nat. Mater. **7**(6), 435–441 (2008).
28. D. Lu and Z. Liu, "Hyperlenses and metalenses for far-field super-resolution imaging," Nat Commun **3**, 1205 (2012).
29. A. Vakil and N. Engheta, "Transformation optics using graphene," Science **332**(6035), 1291–1294 (2011).
30. B. Wang, X. Zhang, F. J. García-Vidal, X. Yuan, and J. Teng, "Strong coupling of surface plasmon polaritons in monolayer graphene sheet arrays," Phys. Rev. Lett. **109**(7), 073901 (2012).
31. A. Grigorenko, M. Polini, and K. Novoselov, "Graphene plasmonics," Nat. Photonics **6**(11), 749–758 (2012).
32. A. Ramasubramaniam, D. Naveh, and E. Towe, "Tunable band gaps in bilayer graphene-BN heterostructures," Nano Lett. **11**(3), 1070–1075 (2011).
33. R. Quhe, J. Zheng, G. Luo, Q. Liu, R. Qin, J. Zhou, D. Yu, S. Nagase, W.-N. Mei, Z. Gao, and J. Lu, "Tunable and sizable band gap of single-layer graphene sandwiched between hexagonal boron nitride," NPG Asia Mater. **4**(2), e6 (2012).
34. I. V. Iorsh, I. S. Mukhin, I. V. Shadrivov, P. A. Belov, and Y. S. Kivshar, "Hyperbolic metamaterials based on multilayer graphene structures," Phys. Rev. B **87**(7), 075416 (2013).
35. M. A. Othman, C. Guclu, and F. Capolino, "Graphene-based tunable hyperbolic metamaterials and enhanced near-field absorption," Opt. Express **21**(6), 7614–7632 (2013).
36. E. H. Hwang and S. Das Sarma, "Dielectric function, screening, and plasmons in two-dimensional graphene," Phys. Rev. B **75**(20), 205418 (2007).
37. E. H. Hwang, S. Adam, and S. D. Sarma, "Carrier transport in two-dimensional graphene layers," Phys. Rev. Lett. **98**(18), 186806 (2007).
38. E. V. Castro, K. S. Novoselov, S. V. Morozov, N. M. Peres, J. M. dos Santos, J. Nilsson, F. Guinea, A. K. Geim, and A. H. Neto, "Biased bilayer graphene: semiconductor with a gap tunable by the electric field effect," Phys. Rev. Lett. **99**(21), 216802 (2007).
39. A. H. Castro Neto, N. M. R. Peres, K. S. Novoselov, and A. K. Geim, "The electronic properties of graphene," Rev. Mod. Phys. **81**(1), 109–162 (2009).
40. A. Andryieuski, A. V. Lavrinenko, and D. N. Chigrin, "Graphene hyperlens for terahertz radiation," Phys. Rev. B **86**(12), 121108 (2012).
41. J. Wang, Y. Xu, H. Chen, and B. Zhang, "Ultraviolet dielectric hyperlens with layered graphene and boron nitride," J. Mater. Chem. **22**(31), 15863–15868 (2012).
42. P. Y. Chen and A. Alù, "Atomically thin surface cloak using graphene monolayers," ACS Nano **5**(7), 5855–5863 (2011).
43. B. Wang, X. Zhang, X. Yuan, and J. Teng, "Optical coupling of surface plasmons between graphene sheets," Appl. Phys. Lett. **100**(13), 131111 (2012).
44. E. Palik, *Handbook of Optical Constants of Solids* (Academic, 1991).
45. J. A. Robinson, M. Labella III, K. A. Trumbull, X. Weng, R. Cavelero, T. Daniels, Z. Hughes, M. Hollander, M. Fanton, and D. Snyder, "Epitaxial graphene materials integration: effects of dielectric overlayers on structural and electronic properties," ACS Nano **4**(5), 2667–2672 (2010).
46. H. Alles, J. Aarik, J. Kozlova, A. Niilisk, R. Rammula, and V. Sammelselg, "Atomic layer deposition of high-k oxides on graphene," in *Graphene–Synthesis, Characterization, Properties and Applications*, J. R. Gong, ed. (InTech, 2011), pp. 99–114.

47. T. Mohiuddin, A. Lombardo, R. Nair, A. Bonetti, G. Savini, R. Jalil, N. Bonini, D. Basko, C. Galiotis, N. Marzari, K. S. Novoselov, A. Geim, and A. Ferrari, "Uniaxial strain in graphene by Raman spectroscopy: G peak splitting, Grüneisen parameters, and sample orientation," Phys. Rev. B **79**(20), 205433 (2009).
48. M. Born and E. Wolf, *Principles of Optics: Electromagnetic Theory of Propagation, Interference and Diffraction of Light* (CUP Archive, 1999).
49. K. S. Novoselov, D. Jiang, F. Schedin, T. J. Booth, V. V. Khotkevich, S. V. Morozov, and A. K. Geim, "Two-dimensional atomic crystals," Proc. Natl. Acad. Sci. U.S.A. **102**(30), 10451–10453 (2005).
50. N. Petrone, C. R. Dean, I. Meric, A. M. van der Zande, P. Y. Huang, L. Wang, D. Muller, K. L. Shepard, and J. Hone, "Chemical vapor deposition-derived graphene with electrical performance of exfoliated graphene," Nano Lett. **12**(6), 2751–2756 (2012).
51. E. Moreau, S. Godey, F. Ferrer, D. Vignaud, X. Wallart, J. Avila, M. Asensio, F. Bournel, and J.-J. Gallet, "Graphene growth by molecular beam epitaxy on the carbon-face of SiC," Appl. Phys. Lett. **97**(24), 241907 (2010).
52. J. Zhang, J. Xiao, X. Meng, C. Monroe, Y. Huang, and J.-M. Zuo, "Free folding of suspended graphene sheets by random mechanical stimulation," Phys. Rev. Lett. **104**(16), 166805 (2010).
53. K.-J. Lee, A. P. Chandrakasan, and J. Kong, "Breakdown current density of CVD-grown multilayer graphene interconnects," IEEE Electron Device Lett. **32**(4), 557–559 (2011).
54. L. Ji, H. Zheng, A. Ismach, Z. Tan, S. Xun, E. Lin, V. Battaglia, V. Srinivasan, and Y. Zhang, "Graphene/Si multilayer structure anodes for advanced half and full lithium-ion cells," Nano Energy **1**(1), 164–171 (2012).

1. Introduction

The diffraction limit of light, caused by the exponential decay of evanescent waves which carry high spatial frequency information, prevents the conventional microscopy imaging below half of light wavelength [1]. To overcome the diffraction limit, near-field scanning optical microscopy has been invented to reach a much finer resolution below the diffraction limit and has led to the possibility of resolving details on the orders of the 10-100 nm scale [2]. However, the major constraint of this invention might be the need for scanning the sample surface point by point, making the entire scanning procedure extremely slow, hence whole imaging cannot be formed in real time.

Emerging within the last decade, the fields of plasmonics and metamaterials have offered exciting solutions for exhibiting many exotic optical phenomena and material properties, such as subwavelength waveguiding [3–8], nanofocusing [9, 10], negative-index of refraction [11, 12], strongly anisotropic materials [13–17], and "trapped rainbow" effect [18–21]. A new super-resolution imaging concept so-called "superlens" has attracted tremendous research interest for its capability of amplifying evanescent waves by use of negative-index material and projecting subdiffraction images without scanning [11, 12]. However, the amplified imaging is within the limit of the near field because the evanescent waves will disappear within a short distance after the negative-index material, hence is undetectable by conventional optics. It is highly desirable for many applications to produce a direct far-field optical image with subwavelength features that can be further processed by conventional optical microscopy. Far-field superlens, consisting of a silver superlens coated with additional nanoscale corrugations on its top surface, was proposed to achieve this goal by projecting a sub-diffraction imaging into the far-field [22]. The evanescent waves can be amplified by the silver superlens, and subsequently, converted into propagation waves via a designed surface corrugation. The far-field images are obtained by retrieving the field angular spectrum, hence it should not be regarded as a direct imaging. Metallic nanowires based subwavelength imaging systems have also attracted intensive research interests for their abilities to achieve far-field sub-diffraction imaging within a wideband frequencies and low-loss [23]. However, it remains a great challenge in creating uniform metallic nanowire arrays as well as introducing of nanoscale gaps between the arrays.

Alternatively, two groups independently proposed optical hyperlens, an anisotropic metamaterial consisting of alternating metal/dielectric multilayer, which has shown the capability of supporting the propagation of evanescent waves due to the hyperbolic dispersion curve [13–17, 24–26]. When evanescent waves enter into such an anisotropic medium, the large transverse wave vectors can be gradually compressed as they propagate outward due to the conservation of angular momentum, projecting a magnified image into the far-field outside the anisotropic medium [13–17, 24–26]. The anisotropic lens has been termed a 'hyperlens' because of the hyperbolic function of the dispersion. Compared with conventional

optics lens, the hyperbolic dispersion curve for a hyperlens need to be designed to be nearly flat to ensure light waves with different transverse wave vectors all propagate with the same phase velocity along the normal direction of stacked layers, which is of great importance in forming undistorted image in the far-field [27, 28]. Apparently, the employment of metal will limit the hyperlens to working at a particular wavelength determined by the filling ratio of dielectric and metal layer because the optical properties of metal cannot be adjusted after fabrication. So far, previous hyperlenses in the infrared or THz range can only be constructed by metallic wires rather than alternating metal/dielectric multilayer. This can be attributed to the fact that metal usually has very large dielectric permittivity relative to dielectric layer in the infrared or THz range, hence forming a hyperbolic dispersion curve based on metal/dielectric multilayer is still challenging.

In contrast to metal, graphene, whose optical response is characterized by surface conductivity, has attracted special attention in optical field since free standing graphene was found [29–39]. Recent study has demonstrated that two-dimensional electrons and holes in graphene respond to an external electric field by screening the external field, i.e., modifying or changing the external field in a complex manner [36–39]. At low frequencies such as mid-infrared range, graphene behaves like a thin metal layer with negative permittivity as the imaginary part of conductivity can be tuned to be positive via external tunability such as electric field, magnetic field, and gate voltage [29, 30]. This unique feature has made graphene a promising candidate for constructing various nanophotonic devices, such as superlens, Luneburg lens and SPP waveguides. Optical hyperlenses for THz and ultraviolet frequency have been theoretically demonstrated by use of graphene wire medium, graphene or boron-nitride layered structures, respectively [40, 41]. Recently, alternating graphene/dielectric multilayer has been demonstrated to be capable of supporting hyperbolic dispersion curve, where the effective dielectric permittivity along radial (ε_r) and tangential direction (ε_θ) are positive and negative, respectively [34]. However, for hyperlens implementation $\varepsilon_r<0$ and $\varepsilon_\theta>0$ is highly desirable.

In this article, considering that the dielectric permittivity of graphene can be tuned to be negative via external tunability, we give a proposal for optical hyperlens for far-field subdiffraction imaging based on alternating graphene/dielectric multilayer in the mid-infrared domain. The thickness of dielectric layer is made comparable to that of graphene layer, leading to hyperbolic dispersion curve with $\varepsilon_r<0$ and $\varepsilon_\theta>0$, which is capable of supporting the propagation of evanescent waves. Numerical simulation results by finite-element method confirm that two point sources with separation far below the diffraction limit can be magnified by the systems to the extent that conventional far-field optical microscopy can further resolve. We also demonstrate such a hyperlens can be made to work in a broadband region due to the flexible tunability of graphene's dielectric permittivity.

In Section 2, we will briefly introduce the working principle for far-field subdiffraction imaging based on alternating graphene/dielectric multilayer. In Section 3, triangle-shaped hyperlens is proposed, and the effect of far-field subwavelength imaging is validated by numerical simulations. In Section 4, we will propose cylindrical hyperlens, and reveal that such a hyperlens can work in a wideband frequency by tuning graphene's relative permittivity via external tunability. In Section 5, we will draw a brief conclusion.

2. Principle of hyperlens based on alternating graphene/dielectric multilayer

In a cylindrical coordinate system the dispersion relationship of electromagnetic wave can be simply described as $k_\theta^2/\varepsilon_r + k_r^2/\varepsilon_\theta = k_0^2$, where k_θ and k_r are wave vectors, ε_θ and ε_r are relative permittivities along tangential and radial directions, respectively [14]. In the k space, this equation represents an ellipse or hyperbola depending on the sign of ε_θ and ε_r. When the sign(ε_θ) is unequal to sign(ε_r), the dispersion curve represents a hyperbola with the asymptotes denoted as $k_r = \pm |\varepsilon_\theta/\varepsilon_r|^{1/2}k_\theta$. As compared to ellipse-shaped dispersion curve, the hyperbolic one has the advantage of supporting the propagation of high frequency components carried by evanescent waves, leading to a subdiffraction imaging in the far-field. To retrieve an undistorted imaging, the hyperbolic dispersion curve should be designed to be very flat to

ensure all the light waves propagate along the radial direction, i.e., ε_θ is close to zero. In other words, the field distribution in an arbitrary plane can be transferred to any other plane point by point without imaging distortion [14]. Generally, such kind of anisotropic material at optical frequencies can be simply realized by use of alternating metal/dielectric multilayer, where the dielectric permittivities of metal and dielectric layer are negative and positive, respectively [13, 14]. If the thicknesses of both layers d_1 and d_2 are much smaller than the operating wavelength, this layered structure can be represented as a uniform anisotropic material with a permittivity tensor given by [14]

$$\varepsilon_{//} = (a_1\varepsilon_1 + a_2\varepsilon_2)/(a_1+a_2), \varepsilon_\perp = (a_1+a_2)\varepsilon_1\varepsilon_2/(a_2\varepsilon_1+a_1\varepsilon_2) \qquad (1)$$

Where $\varepsilon_{//}$ and $\varepsilon_\perp$ denote the permittivities along the tangential and radial directions, respectively. a_1 and a_2 are filling ratios, respectively, and satisfying $a_1 + a_2 = 1$, ε_1 and ε_2 are the permittivities of metal and dielectric layers, respectively.

To realize a hyperlens without distorted imaging, it is highly required that $\varepsilon_{//}>0$, $\varepsilon_\perp<0$ and $\varepsilon_{//}\to0$, hence $\varepsilon_1<0$, $\varepsilon_2>0$, and $a_1\varepsilon_1 + a_2\varepsilon_2\to0$ is highly desirable for a hyperlens. In the ultraviolet and visible range, silver could be chosen as the negative-index material [17, 22]. Nevertheless, in the infrared domain, it is a significant challenge in constructing a hyperlens based on metal owing to its large permittivity and high transmission loss. For example, silver layer has the real part of relative permittivity of −5132.3, and can only support the propagation of electromagnetic wave for a distance of approximately 11 nm at the wavelength of 10 μm.
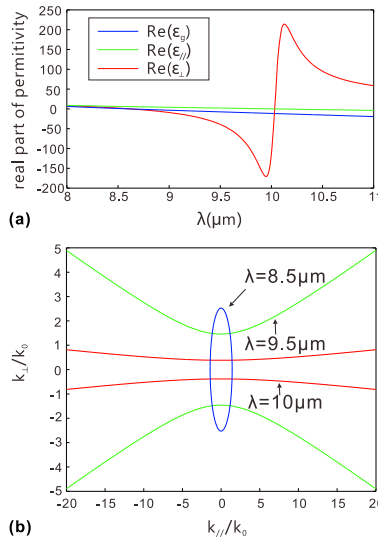

(a)

(b)

Fig. 1. (a) Dependence of the real parts of effective permittivity of graphene layer (blue line), tangential (green line) and radial (red line) permittivities for alternating graphene/dielectric multilayer as a function of wavelength ranging from 8 to 11 μm with $\mu_c = 0.087$ eV. The thicknesses of graphene and dielectric layers are both assumed to be 1 nm. (b) Dispersion relation of hyperlens. Blue line: $\lambda = 8.5$ μm, green line: $\lambda = 9.5$ μm, and red line: $\lambda = 10$ μm.

It's interesting that graphene's permittivity can be tuned to be negative and comparable to that of dielectric layer via external tunability. Similar to a previous theoretical study on plasmonics and metamaterials based on graphene [30, 34, 35, 40, 42, 43], Kubo formula has been widely used to calculate graphene's surface conductivity under the assumption of chemical potential μ_c. In the mid-infrared range with $|\mu_c|\gg k_BT$ (k_B is Boltzmann constant, and T is the temperature), surface conductivity of graphene layer retrieved from Kubo formula could be approximated as [42]

$$\sigma_g = i\frac{e^2 k_B T}{\pi\hbar^2\left(\omega + i\tau^{-1}\right)}\left[\frac{\mu_c}{k_B T} + 2\ln\left(\exp\left(-\frac{\mu_c}{k_B T}\right) + 1\right)\right]$$

$$+ i\frac{e^2}{4\pi\hbar^2}\ln\left[\frac{2|\mu_c| - \hbar\left(\omega + i\tau^{-1}\right)}{2|\mu_c| + \hbar\left(\omega + i\tau^{-1}\right)}\right] \tag{2}$$

Where e is the electron charge, $\hbar$ is the reduced Planck's constant, ω is the radian frequency, τ is the momentum relaxation time representing loss mechanism, and μ_c is the chemical potential. In our study, T = 300 K, τ = 0.5 ps, and μ_c is a variable determined by external electric field bias [43]. To achieve a static electric field bias on graphene, several different schemes have been proposed [29]. As for our graphene/dielectric multilayer structure, to provide an equivalent μ_c on each of graphene layer we can employ a split gate structure to apply an identical bias voltage to different graphene layers, or place a gate electrode on all the graphene layers with a bias voltage [29]. Consequently, the value of μ_c can be tuned by varying the bias voltage. It should be noted, the environment could strongly affect the optical properties of graphene layer due to the field screening [36–39]. However, in this work the surface conductivity for each graphene layer is retrieved using Kubo formula by assuming a chemical potential, which is closely related to the external electric field. Our focus is to propose and analyze the super-resolution imaging properties of a novel hyperlens based on graphene/dielectric multilayer structures themselves. The first and second terms in Eq. (2) correspond to interband electron-photon scattering process and interband one, respectively. Graphene's effective permittivity ε_g can be written as [29, 43]

$$\varepsilon_g = 1 + \frac{i\sigma_g \eta_0}{k_0 \Delta} \tag{3}$$

Where η_0 ($\approx$377 Ω) is impedance of air and Δ is the thickness of graphene. For saving computation time and storage room in the modeling, the thickness of graphene layer is set at Δ = 1 nm. It clearly shows in Fig. 1(a) that the real part of ε_g shifts from positive to negative as λ ranging from 8 to 11μm with μ_c = 0.087 eV. Silicon is selected as the dielectric layer with relative permittivity of ε_d = 11.7, where the absorption loss can be neglected in the mid-infrared range [44]. It is interesting to note here, in this work we have assumed silicon as the dielectric layer to match the effective permittivity of graphene layer. However, graphene's unique properties may degrade dramatically when graphene is in contact with most of materials. It's to say that silicon layers may change electron properties of graphene. Therefore, other materials that do not change graphene's electron properties is highly desirable for a hyperlens, such as hafnium oxide [45, 46]. In this case, far-field subdiffraction imaging could still be realized by adjusting bias voltage to get an appropriate μ_c to satisfy the requirements for a hyperlens. In our work, we set $d_1 = d_2$ = 1 nm ($a_1 = a_2$ = 0.5), where d_1 and d_2, respectively, represent the thicknesses of graphene and silicon. It should be noted here, the dielectric permittivity of silicon layer with 1 nm thickness can be different from that of bulk silicon due to the field screening [36–39]. Therefore, for practical experimental implementation, the dielectric permittivity of thin silicon layer should be estimated by considering the screening properties of graphene. Therefore, to maintain the capability of far-field subdiffraction imaging for graphene/silicon multilayer structure, the effective dielectric permittivity of graphene should be adjusted by modulating μ_c to change graphene's dielectric permittivity to match that of thin dielectric layer. Alternatively, we can also employ silicon layer with a large thickness, whose dielectric permittivity is approximately equal to bulk material. In this situation, we can simply change the effective dielectric permittivity of graphene by varying μ_c to satisfy the condition $\varepsilon_{//}$>0, $\varepsilon_{\perp}$<0 and $\varepsilon_{//}$→0, which makes graphene/silicon multilayer structure to serve as a hyperlens [14].

From Eq. (1) we can simply obtain the real parts of $\varepsilon_{//}$ [Re($\varepsilon_{//}$)] and $\varepsilon_{\perp}$ [Re($\varepsilon_{\perp}$)] for alternating graphene/dielectric multilayer. The dependence of Re($\varepsilon_{//}$) and Re($\varepsilon_{\perp}$) on the incident wavelength is depicted in Fig. 1(a). For $\lambda = 8.5$ μm, such a metamaterial supports an elliptical dispersion curve with Re($\varepsilon_{//}$) = 2.028 and Re($\varepsilon_{\perp}$) = 6.388 [Fig. 1(b)]. Increasing the working wavelength can make the metamaterial support hyperbolic dispersion curve with Re($\varepsilon_{//}$) = −39.13, Re($\varepsilon_{\perp}$) = 2.136 [$\lambda = 9.5$ μm in Fig. 1(b)], and Re($\varepsilon_{//}$) = −113.1, Re($\varepsilon_{\perp}$) = 0.1468 [$\lambda = 10$ μm in Fig. 1(b)], respectively, which is capable of supporting the propagation of evanescent wave. It should be noted here, although this layered structure can work for far-field subdiffraction imaging for both wavelengths, it is more appropriate for imaging without distortion at $\lambda = 10$ μm due to a much flatter dispersion curve.
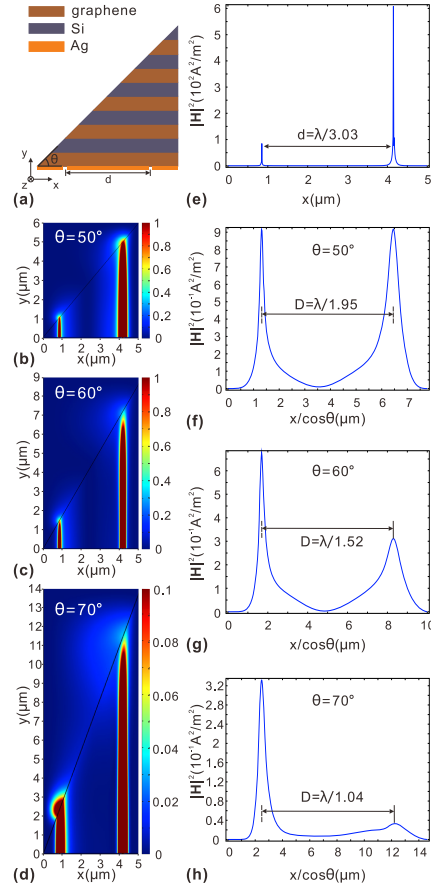
3. Triangle-shaped hyperlens

Fig. 2. (a) Cross-section of triangle-shaped hyperlens based on alternating graphene/silicon multilayer, which is covered with a silver layer (100 nm thick) with two slits (10 nm wide) separated by $d = 3.3$ μm in the bottom, where the two slits serve as two light scatters. The top of the structure is obliquely cut to form a base angle θ. (b-d) Magnetic field distributions of $|(\mathbf{H})|^2$ in the x-y plane: (b) $\theta = 50°$, (c) $\theta = 60°$, and (d) $\theta = 70°$. (e) Magnetic field profile of $|(\mathbf{H})|^2$ at the input plane as the amplitude ratio of the incident light sources is set at 1:7.16. (f-h) Magnetic field profiles of $|(\mathbf{H})|^2$ along the slope surface: (f) $\theta = 50°$, (g) $\theta = 60°$, and (h) $\theta = 70°$.

We first investigate the feasibility of using triangle-shaped alternating graphene/dielectric multilayer for far-field subdiffraction imaging. Figure 2(a) schematically shows the proposed layered structure with an oblique cut on the top, which is covered with a silver layer with two slits in the bottom. To test the effect of far-field subdiffraction imaging, we consider two slits

(10nm width) served as two point sources with separation below the diffraction limit, $d = 3.3$ μm. It should be noted here, other materials that do not change graphene's unique properties, such as hafnium oxide, need to be adopted as the light scatters in actual cases [45, 46]. Figures 2(b)-2(d) shows the magnetic field distributions of $|\mathbf{H}|^2$ in the x-y plane as the amplitude ratio of the incident light sources is set at 1:7.16 [see the magnetic field profile at the input plane in Fig. 2(e)] for different base angles: $\theta = 50°$, $60°$, and $70°$. In the calculations, μ_c is equal to 0.087 eV, which is the same as that is used in Fig. 1(b). The present results show that the light wave propagates straightly along the normal direction of the multilayer, which confirms our prediction in the above analysis. Additionally, the unequal amplitude of the incident light sources in the two slits ensures equal light intensity of two imaging spots at the slope surface with $\theta = 50°$ [Figs. 2(b) and 2(f)]. Through the transfer by the oblique output plane, the image separation, D, will appear to be $d/\cos\theta$. Apparently, one can modulate the base angle to get a proper magnification. The calculated separations between the two output beams at the slope surfaces are $\lambda/1.95$ ($\theta = 50°$), $\lambda/1.52$ ($\theta = 60°$), and $\lambda/1.04$ ($\theta = 70°$), respectively, which are much larger than the diffraction limit [Figs. 2(f)-2(h)]. A larger θ will lead to a greater magnification. The intensity distribution in the far-field zone can then be detected by a conventional optical microscopy. However, the optical paths from different point sources to the imaging plane are different, hence attenuations experienced by different beams are different, which might lead to the variation of imaging intensity and forming a distorted image. This problem can be avoided by use of other shapes of hyperlens, such as cylindrical alternating graphene/dielectric multilayer.
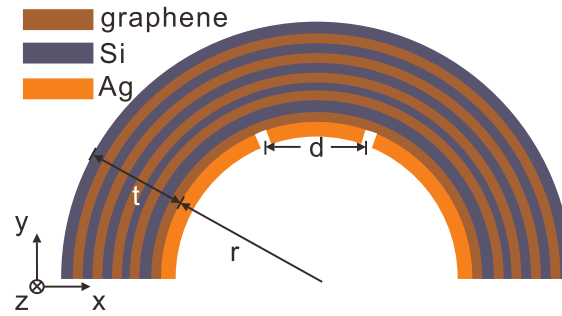
4. Cylindrical hyperlens

Fig. 3. Cross-section of a cylindrical alternating graphene/dielectric multilayer with the thickness t along the radial direction, where the inner surface is coated with a thin silver layer (100 nm thick) with two slits (50 nm wide) separated by $d = 1$ μm. The radius of the inner surface is denoted as r ($= 1$ μm).

Recently, lots of work has been focused on cylinder-shaped hyperlenses, which have been theoretically and experimentally demonstrated to be capable of achieving far-field super-resolution imaging [13, 15]. Apart from being capable of imaging without distortion due to the equal traveling distance for different beams, cylindrical geometry has the advantage of enlarging imaging magnification by enhancing the ratio of the radii of output and input surface, which offers the possibility of resolving details far below the diffraction limit. Figure 3 schematically shows the cross-section of the cylinder-shaped hyperlens, where the inner surface is coated with a thin silver layer with two slits separated by $d = 1$ μm. We can see from Fig. 4(a) that, upon light illumination, light wave from two slits will propagate along the normal direction of the layered structure, and form two imaging spots at the output surface. The distance between the two spots at the output surface is $D = d(r + t)/r$, where r and t, denote the radius of the inner surface and thickness of multilayer, respectively. The image turns out to be enlarged by a factor $(r + t)/r$. Under the plane wave illumination, the field intensities at two imaging points will be equal, hence making an undistorted magnified image in the far-field zone that can be further processed by conventional optical microscopy [Figs. 4(b) and 4(c)]. We have noted in a theoretical study on optical phonons of graphene, bending

of graphene would change graphene's phonon structure, which will change scattering process and modify graphene's conductivity [47]. To effectively minish the influence of phonon scattering process on the surface conductivity of graphene due to curvature, sufficiently large r could be chosen for a cylindrical hyperlens. Meanwhile, we can increase t to maintain a proper imaging magnification factor $(1 + t/r)$. Consequently, we believe that the influence of phonon scattering process due to the curvature on graphene's conductivity can be significantly eliminated for the present hyperlens.
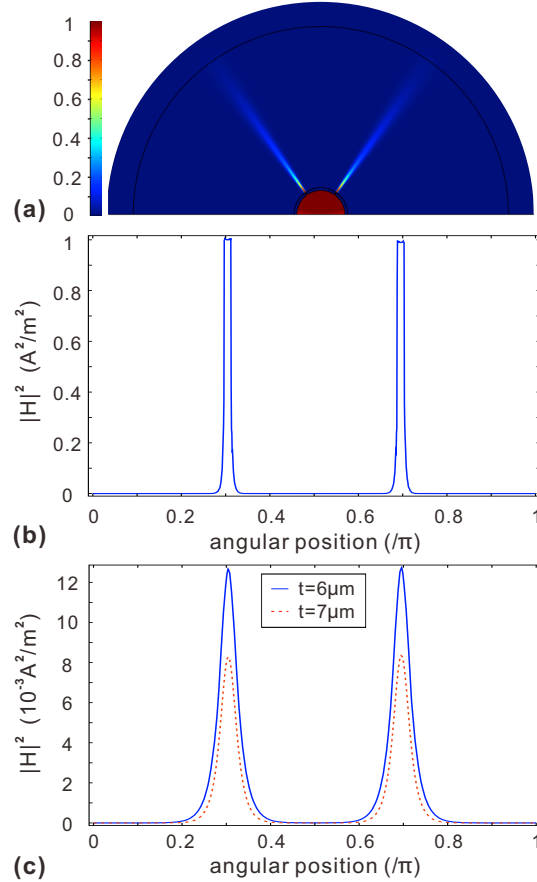
Fig. 4. (a) Magnetic field distribution of $|(\mathbf{H})|^2$ with $t = 6$ μm as the hyperlens is illuminated by a plane wave along y axis, while all the other parameters are the same as those of Fig. 3. (b) Magnetic field profile of $|(\mathbf{H})|^2$ as a function of angle at the input surface with $r = 1$ μm. (c) Magnetic field profiles of $|(\mathbf{H})|^2$ as a function of angle at the output surface with $t = 6$ μm (blue solid line), and $t = 7$ μm (red dashed line), respectively.

If $\varepsilon_{//} \rightarrow 0$ is not strictly satisfied, light wave after the two slits still propagates along the radial direction but with a much larger beam divergence. In this situation, far-field subdiffraction imaging can still be achievable, but the image quality may become worse owing to the mutual interference of the propagation beam. Figures 5(a)-5(c) show the magnetic field distributions of $|H|^2$ with t = 6 μm for different incident wavelengths. We can see that the beam divergence become interferential if the wavelength is assumed to make $Re(\varepsilon_{//})$ much larger than zero [Fig. 5(a)]. Reducing $Re(\varepsilon_{//})$ can significantly decrease the mutual interference at the imaging plane [Fig. 5(b)]. The best image quality can be achievable under the condition $Re(\varepsilon_{//})$ is close to zero [Fig. 5(c)]. In order to quantitatively estimate the effect of mutual interference of beam divergence on the image quality, optical modulation is introduced to represent the image contrast. Generally, optical modulation is defined as the

saddle to peak field intensity $M = I_2/I_1$, where I_2 and I_1 denote the saddle and peak field intensity at the output surface, respectively [48]. It can be seen from Fig. 5(d), the modulation M firstly decreases with the reduced slope of asymptote represented by $\mathrm{Re}(\varepsilon_{//})/\mathrm{Re}(-\varepsilon_\perp)$, and approaches zero as the dispersion curve is nearly flat [$\mathrm{Re}(\varepsilon_{//})/\mathrm{Re}(-\varepsilon_\perp)\to$zero] at $\lambda = 9.85$ μm, where an optimum image quality occurs. We have noted in a recent report on hyperlens based on layered graphene or hexagonal Boron Nitride for far-field imaging in the ultraviolet range, the traveling beams from two point sources mutually interfere significantly because the dispersion curve is not made flat for rectilinear propagation [41].
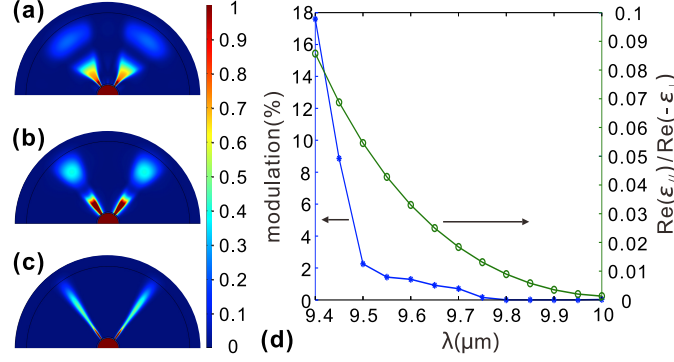

Fig. 5. (a-c) Magnetic field distributions of $|(\mathbf{H})|^2$ for different incident wavelengths: (a) $\lambda = 9.5$ μm ($\varepsilon_g = -7.434 + 0.684i$, $\varepsilon_{//} = 2.137 + 0.342i$, $\varepsilon_\perp = -39.128 + 10.017i$), (b) $\lambda = 9.7$ μm ($\varepsilon_g = -9.032 + 0.6923i$, $\varepsilon_{//} = 1.337 + 0.3461i$, $\varepsilon_\perp = -72.63 + 24.86i$), and (c) $\lambda = 9.9$ μm ($\varepsilon_g = -10.62 + 0.7032i$, $\varepsilon_{//} = 0.5431 + 0.3516i$, $\varepsilon_\perp = -154.4 + 115.1i$). (d) Optical modulation and $\mathrm{Re}(\varepsilon_{//})/\mathrm{Re}(-\varepsilon_\perp)$ versus the incident wavelength ranging from 9.4 μm to 10 μm. For all the simulations, t and μ_c are held constant at 6 μm and 0.087 eV, respectively.
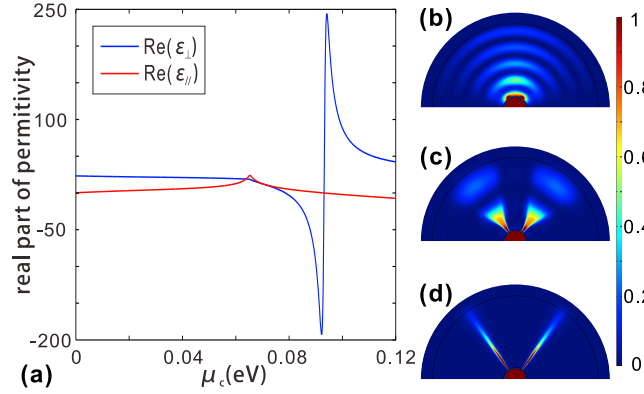

Fig. 6. (a) Dependence of $\mathrm{Re}(\varepsilon_{//})$ and $\mathrm{Re}(\varepsilon_\perp)$ on μ_c for $\lambda = 9.5$ μm. (b-d) Magnetic field distributions of $|(\mathbf{H})|^2$ with $t = 6$ μm and $\lambda = 9.5$ μm for different μ_c: (b) $\mu_c = 0.07$ eV ($\varepsilon_{//} = 12.507 + 0.927i$, $\varepsilon_\perp = 12.515 + 0.808i$), (c) $\mu_c = 0.087$ eV ($\varepsilon_{//} = 2.140 + 0.342i$, $\varepsilon_\perp = -39.023 + 9.984i$), and (d) $\mu_c = 0.093$ eV ($\varepsilon_{//} = 0.057 + 0.315i$, $\varepsilon_\perp = -52.365 + 422.06i$).

After fabrication, alternating metal/dielectric multilayer can work for a hyperlens within a very limited bandwidth around the frequency determined by the filling ratio of metal and dielectric layers. However, alternating graphene/dielectric multilayer is capable of supporting different dispersion curves since graphene's dielectric permittivity can be dynamically modulated by external field. Figure 6(a) shows the dependence of $\mathrm{Re}(\varepsilon_{//})$ and $\mathrm{Re}(\varepsilon_\perp)$ on μ_c at $\lambda = 9.5$ μm. We can divide the dispersion curves into three regions, depending on the sign of $\mathrm{Re}(\varepsilon_{//})$ and $\mathrm{Re}(\varepsilon_\perp)$: (i) $0 \leq \mu_c \leq 0.07861$ eV and 0.09311 eV$<\mu_c\leq0.09316$ eV, where both $\mathrm{Re}(\varepsilon_{//})$ and $\mathrm{Re}(\varepsilon_\perp)$ are positive for an elliptical dispersion curve. However, it is unable to support the

propagation of evanescent wave [see Fig. 6(b)]. (ii) 0.07861 eV<μ_c≤0.09311 eV with Re($\varepsilon_{//}$)>0 and Re($\varepsilon_{\perp}$)<0, which is able to support for a hyperlens [see Figs. 6(c) and 6(d)]. (iii) 0.09316 eV<μ_c≤0.12 eV with Re($\varepsilon_{//}$)<0 and Re($\varepsilon_{\perp}$)>0. The hyperbolic dispersion curve resembles that was reported in previous graphene/dielectric multilayer where a much larger thickness of dielectric layer was adopted in the layered structure [34]. Evidently, it is unable to resolve two diffraction-limited point sources placed along the tangent direction of layered structure.

It should be noted that it is feasible to perform far-field subdiffraction imaging within a broadband frequencies by tuning μ_c to satisfy $\varepsilon_{//}$>0, $\varepsilon_{\perp}$<0 and $\varepsilon_{//}$→0 that is required for a hyperlens without distorted image. For a fixed operating wavelength, one can always choose an appropriate μ_c to meet the above-mentioned requirements that far-field subdiffraction image can be realizable. Simulation results from Fig. 7 show that we are able to achieve far-field super-resolution ranging from 9.2 μm [Fig. 7(a)], 10.2 μm [Fig. 7(b)], 11.2 μm [Fig. 7(c)], 12.2 μm [Fig. 7(d)] with μ_c varied from 0.0965 eV, 0.085 eV, 0.075 eV, 0.067 eV, respectively.
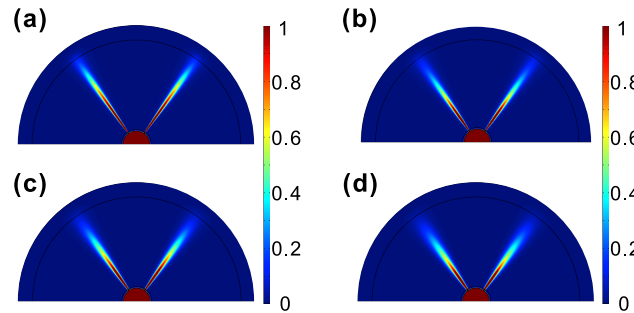

Fig. 7. Broadband far-field subdiffraction imaging by tuning μ_c to satisfy $\varepsilon_{//}$>0, $\varepsilon_{\perp}$<0 and $\varepsilon_{//}$→0:
(a) λ = 9.2 μm (μ_c = 0.0965 eV, $\varepsilon_{//}$ = 0.1419 + 0.2933i, $\varepsilon_{\perp}$ = −159.8 + 378.6i), (b) λ = 10.2 μm (μ_c = 0.085 eV, $\varepsilon_{//}$ = 0.1058 + 0.3709i, $\varepsilon_{\perp}$ = −74.07 + 341.7i), (c) λ = 11.2 μm (μ_c = 0.075 eV, $\varepsilon_{//}$ = 0.4481 + 0.4678i, $\varepsilon_{\perp}$ = −122.9 + 152.8i) and (d) λ = 12.2 μm (μ_c = 0.067 eV, $\varepsilon_{//}$ = 0.761 + 0.5831i, $\varepsilon_{\perp}$ = −90.05 + 86.94i), respectively.

Finally, it is technologically achievable to fabricate layered structure consisting of alternating graphene/dielectric layers, where the dielectric layer is made infinitesimally thin. We can employ cleavage technique [49], chemical vapor deposition (CVD) [50], as well as molecular beam epitaxy [51] methods to implement fabrication of single graphene layer. Recently, fabrication of graphene layered structures, such as the folding of graphene sheets by mechanical deformation and 10-20nm graphene films by CVD growth, has been reported [51–53]. Three-dimensional composites of graphene not only present excellent flexibility that can be bent, stretched, and twisted without breaking, but also preserve the optical properties of two-dimensional graphene. For future experimental implementation of such graphene/silicon multilayer based hyperlenses, deposition techniques (e.g., sputtering and/or E-bean evaporation) can be employed to form the silver layer. The graphene/silicon multilayer structures above the silver layer can be fabricated through a repeated process of filtering liquid-phase exfoliated graphene film and the subsequent coating of silicon film via plasma-enhanced chemical vapor deposition (PECVD) method [54]. In a series of studies, heterostructures composed of alternating graphene/hexagonal Boron Nitride have been already experimentally fabricated [32, 33]. Hexagonal Boron Nitride, which has thickness that is comparable to graphene layer and relative permittivity around 4, can be employed to serve as the dielectric layer. Consequently, we believe that such a graphene/dielectric layered structure might be "designed" freely based on the current nanofabrication technologies in the near future.

5 Conclusions

In conclusion, we have proposed a novel hyperlens based on alternating graphene/dielectric layers for far-field sub-resolution imaging at mid-infrared frequencies. The dispersion curve for such a scheme can be tuned to be hyperbolic by modulating graphene's permittivity to be negative via external electric field. Due to the hyperbolic dispersion curve, such a structure is capable of supporting the propagation of evanescent wave with very large wave vector, hence projecting an amplified far-field image in the far-field region that can be further manipulated by conventional optics systems. Triangular and cylindrical geometries have been employed to validate the imaging effect and were numerically demonstrated to be capable of resolving two point sources that is separated far below the diffraction limit. We have also demonstrated the possibility of achieving broadband far-field subdiffraction imaging without distortion by varying graphene's dielectric permittivity to get a nearly flat dispersion curve for different wavelengths. The present results enable the potential applications in real-time super-resolution imaging, nanolithography, and sensing.